Earth and Planetary Science Letters 452 (2016) 79–89

Contents lists available at ScienceDirect

Earth and Planetary Science Letters

www.elsevier.com/locate/epsl

Interaction between climate, volcanism, and isostatic rebound in Southeast Alaska during the last deglaciation

Summer Praetorius [a,b,*], Alan Mix [a], Britta Jensen [c,d], Duane Froese [c], Glenn Milne [e], Matthew Wolhowe [a], Jason Addison [f], Fredrick Prahl [a]

[a] College of Earth, Ocean & Atmospheric Sciences, Oregon State University, Corvallis, OR 97331, USA
[b] Department of Global Ecology, Carnegie Institution for Science, Stanford, CA 94305, USA
[c] Dept. of Earth and Atmospheric Sciences, University of Alberta, Edmonton, AB, T6G 2E3, Canada
[d] Royal Alberta Museum, 12845 102 Avenue, Edmonton, AB, T5N 0M6, Canada
[e] Dept. of Earth Sciences, University of Ottawa, Ottawa, ON, K1N 6N5, Canada
[f] U.S. Geological Survey, 345 Middlefield Rd., MS 910, Menlo Park, CA 94025, USA

ARTICLE INFO

Article history:
Received 22 September 2015
Received in revised form 16 July 2016
Accepted 18 July 2016
Available online 9 August 2016
Editor: T.A. Mather

Keywords:
paleoclimate
deglaciation
volcanism
isostatic rebound
Alaska
Mt. Edgecumbe

ABSTRACT

Observations of enhanced volcanic frequency during the last deglaciation have led to the hypothesis that ice unloading in glaciated volcanic terrains can promote volcanism through decompression melting in the shallow mantle or a reduction in crustal magma storage time. However, a direct link between regional climate change, isostatic adjustment, and the initiation of volcanism remains to be demonstrated due to the difficulty of obtaining high-resolution well-dated records that capture short-term climate and volcanic variability traced to a particular source region. Here we present an exceptionally resolved record of 19 tephra layers paired with foraminiferal oxygen isotopes and alkenone paleotemperatures from marine sediment cores along the Southeast Alaska margin spanning the last deglacial transition. Major element compositions of the tephras indicate a predominant source from the nearby Mt. Edgecumbe Volcanic Field (MEVF). We constrain the timing of this regional eruptive sequence to 14.6–13.1 ka. The sudden increase in volcanic activity from the MEVF coincides with the onset of Bølling–Allerød interstadial warmth, the disappearance of ice-rafted detritus, and rapid vertical land motion associated with modeled regional isostatic rebound in response to glacier retreat. These data support the hypothesis that regional deglaciation can rapidly trigger volcanic activity. Rapid sea surface temperature fluctuations and an increase in local salinity (i.e., $\delta^{18}O_{sw}$) variability are associated with the interval of intense volcanic activity, consistent with a two-way interaction between climate and volcanism in which rapid volcanic response to ice unloading may in turn enhance short-term melting of the glaciers, plausibly via albedo effects on glacier ablation zones.

1. Introduction

Volcanism may induce short-term (sub-decadal) atmospheric cooling, deplete ozone, and affect the hydrologic and carbon cycles (McCormick et al., 1995; Robock, 2000, 2002). On longer timescales of centuries to millennia, global episodes of enhanced volcanism have been associated with deglaciation, hypothetically in response to gravitational unloading during high latitude ice loss (Hammer et al., 1980; Zielinski et al., 1997; Maclennan et al., 2002; Huybers and Langmuir, 2009; Kutteroff et al., 2013). Debate continues on the magnitude of this effect (Huybers and Langmuir, 2009; Watt et al., 2013), and on the response time of volcanism to isostatic triggering, ranging from nearly instantaneous (Maclennan et al., 2002) to several thousand years (Kutteroff et al., 2013; Watt et al., 2013; Rawson et al., 2016). Most studies have cataloged global or hemispheric averages of eruptive events; these have a statistical advantage of integrating many individual events but a disadvantage of greater uncertainty in the timing of ice unloading for various source regions, making it difficult to assess the triggers and mechanisms responsible for enhanced frequency of deglacial eruptions.

The climatic response to volcanism is similarly complex and difficult to predict, with the potential for global warming related to enhanced CO_2 emissions (Huybers and Langmuir, 2009) or regional lowering of albedo from tephra deposition on snow or ice (Conway et al., 1996), and for regional or hemispheric cooling due to aerosol

* Corresponding author at: Department of Global Ecology, Carnegie Institution for Science, Stanford, CA 94305, USA.
E-mail address: spraetorius@carnegiescience.edu (S. Praetorius).

http://dx.doi.org/10.1016/j.epsl.2016.07.033
0012-821X/

radiative effects in the atmosphere (Robock, 2000) or global cooling by tephra-fertilized marine CO_2 drawdown (Langmann et al., 2010). Each of these processes occurs with its own characteristic timescale, and the type and degree of climate response is likely sensitive to the location, magnitude, composition, and climatic context of a given eruption. Furthermore, the relatively limited spatial extent of macro-tephra fallout and the short-term nature of these events make it difficult to identify and link a geologic record of a climate response to a given volcanic eruption. Nevertheless, it is likely that volcanism may be an important source of abrupt climate forcing, which may help to trigger instabilities in the climate system.

Ice cores preserve a detailed record of climate changes in conjunction with fine-scale tephra and sulfate layers that can record distant eruptions. For example, the GISP2 ice core in Greenland documents enhanced volcanic sulfate deposition during the last deglaciation (17–6 ka) relative to the last 100,000 yrs (Zielinski et al., 1996, 1997). Some of these sulfate peaks have been linked to eruptions from Iceland (Mortensen et al., 2005), which show enhancement of volcanic frequency of up to 50 times modern levels during the last deglaciation (12–10 ka) (Maclennan et al., 2002). While the Greenland record may be biased towards Icelandic volcanism (for example; Bourne et al., 2015) the GISP2 volcanic sulfate record documents an increase in volcanism commencing earlier than peak volcanism on Iceland, leaving the sources of this early deglacial volcanism poorly constrained. Many of the tephra deposits that have been analyzed in Greenland ice cores have compositions distinct from Icelandic volcanoes, suggesting more distal sources such as Japan, Kamchatka, the Cascades of the US Pacific Northwest, or volcanic systems of mainland Alaska or the Aleutian Arc (Mortensen et al., 2005; Abbott and Davies, 2012; Coulter et al., 2012; Jensen et al., 2014; Bourne et al., 2016). Resolving regional volcanic histories and tephra stratigraphies will not only help to constrain the timing and magnitude of the response of distinct volcanic systems to deglacial processes, but could also identify the source regions of volcanic activity recorded in distal archives.

A sequence of at least 12 postglacial tephra deposits from the Mt. Edgecumbe Volcanic Field (MEVF) have been previously identified in terrestrial outcrops, lake sediment cores, and peat cores from Southeast Alaska (Riehle et al., 1992a, 1992b; Beget and Motyka, 1998). A maximum of 28 tephra beds in a terrestrial outcrop have been identified, although the lack of sediment deposition between layers makes it difficult to determine how many of these beds were distinct eruptions as opposed to multiple eruptive phases of a single event. A number of tephras have also been detected in proximal marine sediment cores, some of which have been correlated to the MEVF deposits (Addison et al., 2010).

The postglacial eruptive sequence from the MEVF encompasses a wide compositional range from early basalt flows to rhyolitic tephras later in the sequence; whole-rock geochemistry from previously identified post-glacial MEVF deposits range from basaltic (~49.5 SiO_2 wt%) to rhyolite (~72 SiO_2 wt%) (Riehle et al., 1992b, 1994). Although mafic non-MEVF vents have been identified throughout Southeast Alaska, both terrestrially (Eberlein and Churkin, 1970) and in the submarine environment (Greene et al., 2011), many of these deposits have poor associated age control, limited geochemistry, and all are over 100 km distant (Riehle et al., 1992b). A distinctive dacitic tephra from Mt. Edgecumbe (MEd) dated to near the Pleistocene–Holocene boundary has been well dated on land at 13.13 ± 0.09 ka cal based on ^{14}C dates of 11.25 ± 0.05 ka, Beget and Motyka (1998), recalibrated here using INTCAL13 (Reimer et al., 2013). However, the initiation and duration of the entire MEVF deglacial eruptive sequence is not fully constrained because the land records generally lack good age controls.

Here we utilize rapidly accumulating marine sediments from the Southeast Alaska continental margin to construct a stratigraphically complete and precisely-dated record of the deglacial eruptive sequence from the Southeast Alaska volcanic province at multi-decadal resolution, paired with climate proxies in the same samples. These records provide the highest resolution deglacial multi-proxy climate history of the high-latitude North Pacific to date, and allow for an in-depth evaluation of the interactions among regional climate, glaciation, and volcanism.

2. Methods

2.1. Stratigraphy

Two nearby marine sediment cores were used to form a high-resolution composite record of planktonic oxygen isotopes spanning the late glacial to Holocene period (18.2–4.3 ka) (Praetorius and Mix, 2014). These sediment cores, EW0408-66JC (58.87°N, 137.10°W, 426 m) and EW0408-26JC (56.96°N, 136.43°W, 1623 m) are located in proximity to the MEVF (Fig. 1) and record a combined sequence of ~22 tephras during the deglacial period. Core EW0408-26JC spans 18.2–13.5 ka and records 15 tephra layers in non-bioturbated sediments with high sedimentation rates (100–800 cm/kyr) (Fig. 2). Visual evidence for bioturbation is present in the upper 27 cm of this core, making detection of discrete tephra layers difficult, but rhyolitic tephra shards are present in the sediments. The 48 cm trigger core from site EW0408-26TC is used to extend the record into the Holocene, but low sedimentation rates and bioturbation in these uppermost sediments preclude a well-constrained age stratigraphy. Two tephras were analyzed from core EW0408-26TC at depths of 6–7 cm and 47–48 cm. Core EW0408-66JC spans 13.5–4.3 ka, with sedimentation rates ranging from 200–2000 cm/kyr during the deglacial period and 10 cm/kyr during the Holocene, and is thus used to extend the regional climate and tephra history into the mid Holocene. Two tephras were analyzed from core EW0408-66JC at depths of 858–860 cm and 1374–1376 cm.

2.2. Age model

The age model for these cores (Praetorius and Mix, 2014) consists of 28 radiocarbon dates on mixed planktonic foraminifera (predominantly *Neogloboquadrina pachyderma* (Nps) and *Globigerina bulloides* (Gb)) picked from the >150 μm size fraction (Fig. 2). Calendar corrections were made using the Calib 7.0 calibration software with the Marine13 calibration curve (Reimer et al., 2013). A tephra layer in core EW0408-66JC is matched (based on major element chemistry and stratigraphy; Fig. S3) to a terrestrial tephra layer from Mt. Edgecumbe. This provides an additional age control and an estimate of the marine reservoir correction in core EW0408-66JC during the deglacial interval. A surface–ocean marine reservoir correction of 595 ± 50 yrs (i.e., $\Delta R = 190 \pm 50$ yr in CALIB 7.0/Marine13) was applied to core EW0408-66JC based on the difference between the terrestrial radiocarbon age for the Mt. Edgecumbe dacite deposit and the planktonic foraminifera radiocarbon ages bracketing the dacite deposit in EW0408-66JC (Fig. 2). A marine reservoir correction of 735 ± 50 yrs (i.e., $\Delta R = 330 \pm 50$ yr in CALIB 7.0/Marine13) was applied to core EW0408-26JC based on the average age difference between terrestrial plant material and marine bivalves from a nearby core site (Addison et al., 2010).

An alternative age model was produced by correlating the oxygen isotope changes in the GOA record to the NGRIP chronology to allow for small changes in the marine reservoir age (Praetorius and Mix, 2014). This tuned age model preserves 15 of the original radiocarbon dates, the age control provided by the MEd correlation, and includes 5 adjusted tie points within the time period from 13.5–11.7 ka that result in only minor (<200 yrs) changes to

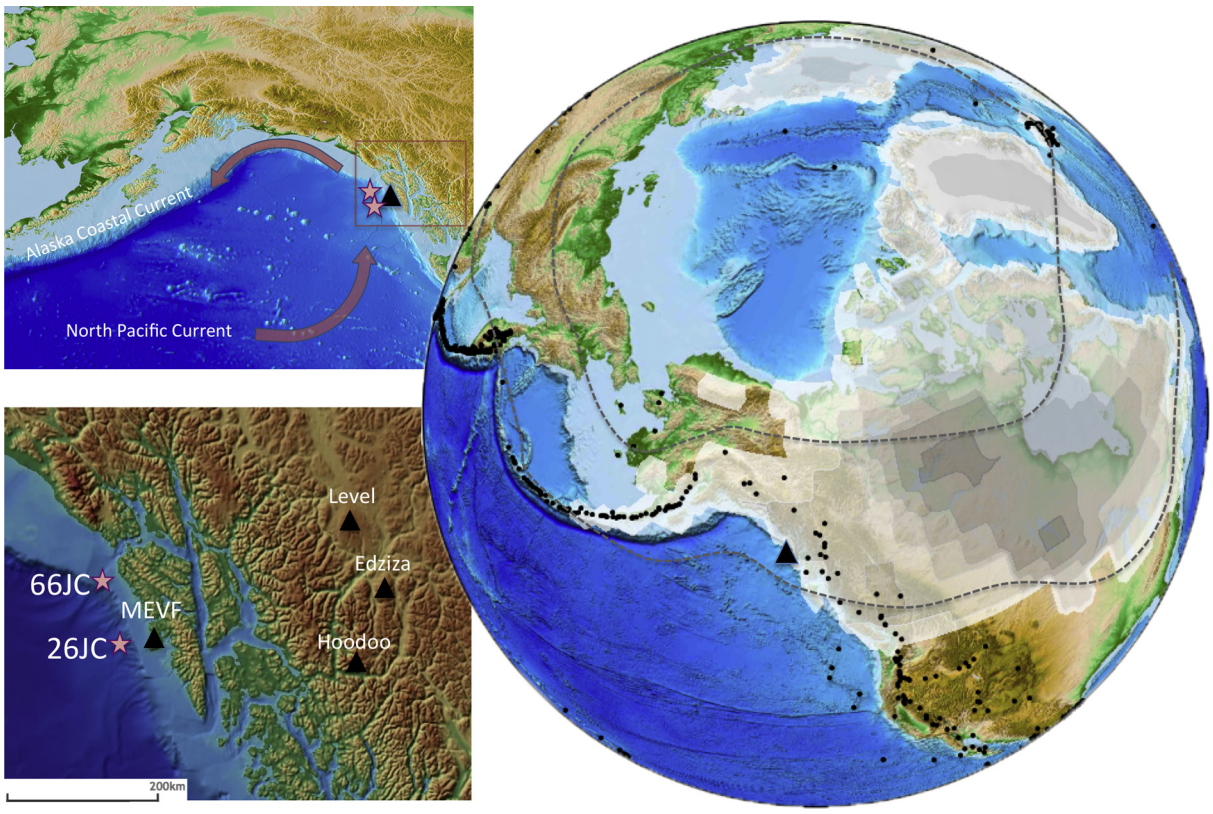

Fig. 1. Gulf of Alaska study area. Large map shows the distribution of volcanoes (black dots) in the northern hemisphere, along with the areal extent and height of the ice sheets at the last glacial maximum (Peltier, 2004). The location of Mt. Edgecumbe is indicated (black triangle), along with the modeled ash dispersal from the 1912 Alaskan Katmai eruption (Welchman, 2012). The inserts show a more detailed view of the GOA study area, with major surface currents and the locations of marine sediment cores EW0408-66JC (58.87°N, 137.10°W, 426 m) and EW0408-26JC (56.96°N, 136.43°W, 1623 m) (purple stars). Nearby volcanoes of the northern Cordilleran volcanic field (NCVF) are also identified. (For interpretation of the references to color in this figure legend, the reader is referred to the web version of this article.)

the original age model, indicating relatively constant marine reservoir ages in this region throughout the deglaciation (Fig. 2). We adopt the tuned chronology in the records presented here in order to evaluate the timing of the MEVF eruptions relative to those recorded in the Greenland ice cores, although we note that the conclusions of the paper are not sensitive to the choice between these age models, as four of the five tie points used in constructing the tuned age model occur after the tephra sequence. Extensive details for these age models can be found in Praetorius and Mix (2014).

2.3. Tephra analysis

Twenty-three tephra samples were analyzed for major element concentrations of glass (calculated as oxides) in cores EW0408-66JC, EW0408-26JC, and EW0408-26TC, but four of the twenty-three samples analyzed have limited geochemical data (Fig. 2, Table S1) due to either a small number of glass shards or the presence of heavily microlitic glass that prevented the acquisition of pure glass analyses. Tephra analyses were conducted at University of Alberta by wavelength dispersive electron microprobe analysis (WDS-EMPA) on a JEOL 8900 Superprobe. Each analysis represents a single glass shard, and tabulated data are averages and distributions. On average the samples contain 15 shard analyses. For detailed sample preparation methods see (Jensen et al., 2008).

Analytical conditions were chosen to minimize Na-loss and include a defocused beam of 10 μm, a 6 nA current and 15 KeV voltage. Calibration is by natural mineral and glass standards. Two secondary standards of known composition, the Old Crow tephra and Lipari obsidian ID 3506 (Kuehn et al., 2011), were analyzed at the start and end of each day, as well as after every ∼100 analyses, to assess the quality of calibration, track potential instrumental drift, and allow accurate comparison between datasets collected on different days. All data are normalized to 100% on a volatile and water-free basis, non-zero values are included in averages, and individual analyses are available in Supporting Data.

2.4. Alkenone measurements

Total lipids were extracted from selected intervals of freeze-dried sediment (∼5 g) from EW0408-66JC and EW0408-26JC with a 3:1 mixture of methylene chloride:methanol using a Dionex ASE-200 automated solvent extraction system and the extracts subsequently partitioned into hexane (Walinsky et al., 2009). Total lipid extracts were separated into adducted (alkenone-containing) and non-adducted fractions using a standard urea adduction technique (Christie, 2003). The alkenone-containing fraction was characterized quantitatively by capillary gas chromatography with flame ionization detection (Walinsky et al., 2009). Uncertainties in the quantification of di-unsaturated (K37:2) and tri-unsaturated (K37:3) alkenones were conservatively treated as the sum of an average baseline variability component (dominates error in low-abundance samples) and a 5% uncertainty in the integrated area (dominates in high-abundance samples). These uncertainties were then propagated into calculation of the $U^{K'}_{37}$ temperature index (Prahl et al., 1988).

2.5. Surface ocean $\delta^{18}O_{sw}$ records

The planktonic foraminiferal δ^{18}O records, when corrected for $U^{K'}_{37}$ temperature (using empirical δ^{18}O:temperature relationships

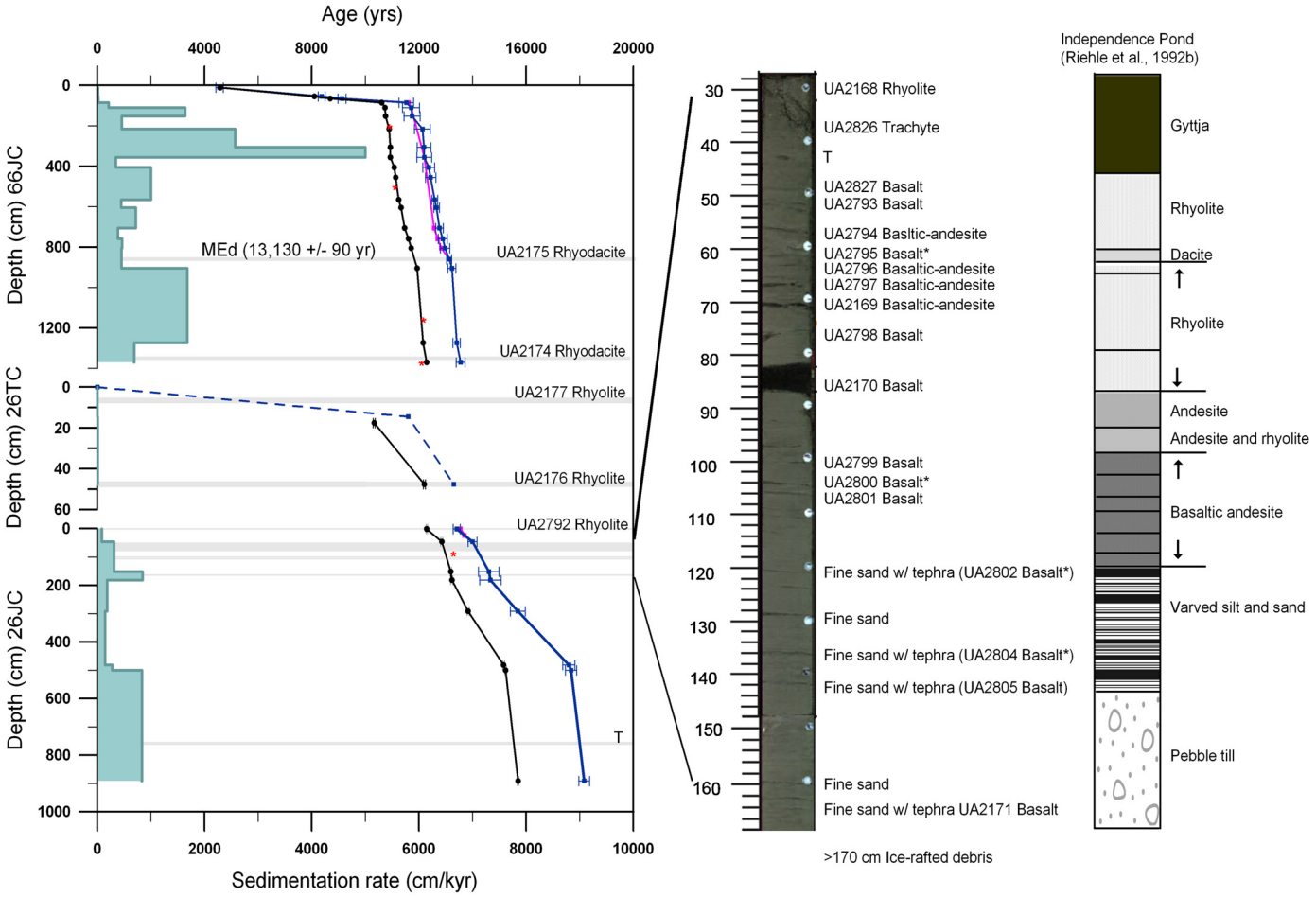

Fig. 2. Age Models for cores EW0408-66JC and EW0408-26JC/TC (Praetorius and Mix, 2014). Black dots are radiocarbon ages on mixed planktonic foraminifera. Analytical uncertainties for the radiocarbon analysis are smaller than the symbols used in the plot (typically 20–50 yrs). The red stars are radiocarbon dates excluded from the age model due to small age reversals. The blue squares represent the calibrated midpoint age BP (1950), with $\pm 2\sigma$ uncertainty bars, using the Calib 7.0 software with the Marine13 calibration curve (Reimer et al., 2013). A tuned age model was also generated based on correlation to the NGRIP $\delta^{18}O$ record, and results in only minor adjustments to the original calibrated ^{14}C age model (pink lines). The age model for EW0408-26TC (blue dotted line) is based on one calibrated radiocarbon date near the base of the core, two isotopic tie points to core EW0408-66JC, and a designated modern core top age. The 23 tephra samples that were analyzed are labeled with their lab code and general compositions. A core photo of EW0408-26JC is shown for the depth 28–170 cm. Samples denoted with $*$ represent the analyses that did not have enough ash shards or smooth glass surfaces for adequate geochemical classification. Tephra layers present but unanalyzed are denoted with a T. The inferred Mt. Edgecumbe dacite (MEd) is indicated with its calibrated age (Beget and Motyka, 1998). A stratigraphic sequence of the MEVF postglacial tephras from Independence pond, as outlined in Riehle et al. (1992b) is shown for comparison with the marine sequence. (For interpretation of the references to color in this figure legend, the reader is referred to the web version of this article.)

in Bemis et al., 1998) and ice-volume (based on Waelbroeck et al., 2002) provide an estimate of changing oxygen isotopic composition of seawater ($\delta^{18}O_{sw}$) related mostly to changes in near-surface regional salinity. The primary cause of regional salinity variations here is freshwater runoff from precipitation and glacial meltwater. Due to the different core locations of Sites EW0408-66 and EW0408-26, empirical corrections were made to the $\delta^{18}O$ and paleotemperature records for core EW0408-66JC based on average differences for overlapping time intervals in EW0408-66JC and trigger core EW0408-26TC in order to form the composite records (see Supplementary Information for further details).

2.6. Isostatic adjustment modeling

The isostatic response leading to regional changes in relative sea level (RSL) was computed using a model of glacial isostatic adjustment (GIA). This model has two input components: a loading model of changes in ice extent through time and an Earth model to define the parameters that govern the isostatic deformation due to the ice history. The model also accounts for the loading associated with changes in RSL using the theory outlined in Mitrovica and Milne (2003) and the algorithm described in Kendall et al. (2005). GIA-induced perturbations in Earth rotation are also included in the model simulations (Milne and Mitrovica, 1998; Mitrovica et al., 2005).

We use the ICE-5G model (Peltier, 2004) to define the ice loading history. This model has been tuned to fit a number of observational constraints around the globe including ice extent limits and RSL curves in North America (see Peltier, 2004 for further details). The Earth model is spherically symmetric and assumes a Maxwell (visco-elastic) rheology. The density and elastic structure are taken from seismic constraints (Dziewonski and Anderson, 1981). The viscous structure is less precisely known and so is parameterized into three layers: an outer shell of very high viscosity to simulate the lithosphere as a thin elastic shell; an upper mantle region of uniform viscosity from the base of the lithosphere to ~670 km depth; a lower mantle region from this depth to the core-mantle boundary (~2900 km). The viscosity parameters considered in this study are defined in Table S2. We note that the ICE-5G model was developed assuming a particular Earth viscosity model (VM2; Peltier, 2004) in which the viscosity structure is defined with greater depth resolution than those described above. This viscosity model is also considered in our analysis.

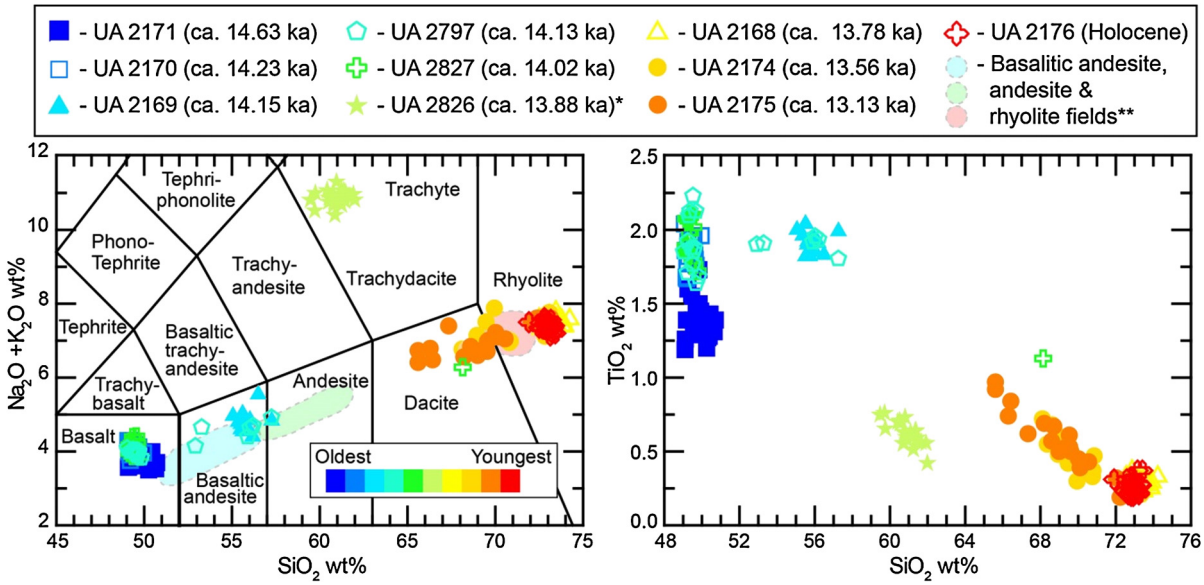

Fig. 3. Total alkali-silica (TAS) (after LeBas et al., 1986) and Harker diagrams of tephras analyzed in this study. Only 10 of 19 tephras are included for clarity sake, samples have been chosen to represent each main compositional group. The MEVF tephra set starts with basalts and basaltic-andesites, and progressively moves into higher SiO_2 content tephras, ending with dacites and rhyolites. The order of this sequence is consistent with the terrestrial sequences. The average age uncertainty for the tephra dates are ±200 yrs. Two types of basalts are present in the tephra sequence and are most clearly differentiated by TiO_2 wt%.
*UA 2826 most likely originates from the northern Cordilleran volcanic field.
**Fields define whole-rock geochemistry of main post-glacial fallout deposits, adapted from Fig. 8 in Riehle et al. (1992b).

2.7. Ice rafted debris and tephra

A record of ice-rafted debris (IRD) was generated by counting the non-volcanic sand and gravel grains >600 μm in each sample and normalizing these counts relative to the dry bulk sample sediment weight. Grains of this size can only be delivered to the deep-sea through transport and subsequent fallout from icebergs. Tephra shards >600 μm were similarly counted for each sample; the presence of such large shards suggests a proximal source for the ejecta.

Counts of these large grains may miss finer grained material. Conducting individual grain counts in the 125–600 μm fraction for each sample was time-prohibitive, therefore we use the coarse fraction weight percent as a more continuous proxy for the delivery of grains >125 μm, which is dominated by IRD and tephra with only trace contributions from microfossils or other biogenic debris. Based on qualitative microscopic observations, timing of the shift from IRD-dominated to tephra-dominated >125 μm coarse fraction is precisely aligned with the divide between IRD and tephra dominance in the >600 μm fraction.

2.8. Greenland volcanic sulfate record

We compare the regional Southeast Alaska tephra record to hemispheric measures of volcanism documented in ice cores. The Second Greenland Ice Sheet Project (GISP2) volcanic sulfate record (Zielinski et al., 1996) is used here as a proxy for explosive volcanism in the northern hemisphere. The temporal resolution of this record is higher for the Holocene (individual samples cover approximately 2 yr intervals) than for the deglacial interval (individual samples cover 3–10 yr), therefore the frequency of deglacial volcanic events is underrepresented relative to the Holocene, although the average volcanic sulfate concentration is relatively robust on the century scale. Thus, to estimate long-term variations in explosive volcanism from the Greenland ice core data, we calculated a 200-yr binned average volcanic sulfate concentrations throughout the past 20 ka from GISP2, then calculated average sulfate fluxes in these bins, correcting for strain related layer thinning as a function of depth (following Alley, 2000a, 2000b) with ages adjusted to the GICC05 age model (Rasmussen et al., 2006). Although this record is biased toward sulfur-rich eruptions and may miss some smaller or more distal events, it provides a useful measure of the large-scale explosive volcanic input to the northern-hemisphere atmosphere.

3. Results

3.1. Tephra stratigraphy

All but one of the marine tephra layers that were analyzed are compositionally and stratigraphically consistent with the terrestrial tephra sequence from the MEVF (Riehle et al., 1992a), which includes an orderly progression of basaltic, basaltic andesitic, rhyolitic, and rhyodacitic tephras (Fig. 2, Fig. 3). This compositional trajectory is thought to reflect a basaltic magma chamber underlying a silicic magma chamber. Early mafic products erupted through a series of vents aligned along a crustal fissure in the MEVF, and later silicic eruptions emanated from the central vents of Crater Ridge and Mt. Edgecumbe (Riehle et al., 1992b).

Our analyses show that earliest tephra layers are basalts and basaltic-andesites within the age range of 14.6–14.0 ka (Fig. 2). Similar geochemistry and limited data among some samples make it difficult to determine unambiguously how many of the deposits were independent eruptions as opposed to potentially redeposited material. However, many of the tephra layers have unique morphologies (such as granular basalt versus basalt glass shards), two types of basalt can be geochemically differentiated (Fig. 3; Table S1), and some are multi-modal, all of which suggests that most units represent multiple, closely-spaced, eruptions during this ~600 yr interval. Most samples are preserved within laminated sediments, excluding the possibility that bioturbation moved a single ash into multiple burrows. This early interval of rapid tephra deposition also occurs after the disappearance of large IRD grains, arguing against redeposition from ice rafting. Fine sand turbidite deposits are present within the transition zone between large IRD deposition and the onset of rapid

tephra deposition (105–165 cm), so some of the early ash layers may have been emplaced within turbidites sourced from shallow water (Horn et al., 1969). These ash eruption and turbidite events may have been essentially coeval, as both may be associated with regional seismicity (Goldfinger, 2011).

Several lines of evidence support that the MEVF is the dominant source of tephra in this proximal offshore region. The general progression of the geochemistry from mafic to felsic mirrors terrestrial deposits (Fig. 3), terrestrial and marine ages are in agreement, and grain-sizes of the deposits are too coarse for distal sources such as the Aleutians. Postglacial MEVF terrestrial outcrops include basalt flows, and up to 20 basaltic–andesitic, seven andesitic, and at least one dacitic and six rhyolitic pyroclastic fallout units (Riehle et al., 1992b). The whole-rock geochemistry of the pyroclastic units are compositionally similar to the tephras in the offshore record (Fig. 3; Riehle et al., 1992b). Any geochemical offset in the data between whole-rock analyses of the pyroclastic units and the glass analyses are as expected. For example, plagioclase is the dominant mineral in all deposits, with SiO_2 averaging around 52 wt% (Riehle et al., 1992b). Therefore glass analyses for the basaltic-andesites will tend to have lower average SiO_2 wt% due the exclusion of the plagioclase, and glass analyses on rhyolites will have a higher SiO_2 wt% (see Fig. 3). The offshore record may be missing some basaltic-andesitic and andesitic units reported by Riehle (e.g. 1992b), although andesites are present but underrepresented geochemically because they tend to consist of heavily microlitic glass that limits glass analyses (e.g. UA2795, UA2827, see supplementary data). There is also the possibility that the marine record may include basaltic fallout from the oldest post-glacial basalt flows that have limited exposure on land (see Riehle et al., 1992b, 1994 for details).

One tephra analyzed (UA2826) is geochemically unique; its high alkali content categorizing it as a trachyte (Fig. 3). The only known nearby source for tephras of this composition is the northern Cordilleran volcanic field (NCVF) in British Columbia. This region contains several large volcanoes that were active in the latest Pleistocene and Holocene, including Edziza, Hoodoo and Level Mountains, all of which are approximately 300 km to the east of the MEVF (Fig. 1) (Edwards and Russell, 2000). All three of these volcanoes have erupted trachytes during past activity (Souther, 1992; Edwards and Russell, 2000).

A 4-cm thick rhyolite deposit in marine core EW0408-26JC occurs at 13.78 ka (UA2168). Above (i.e., younger than) this tephra deposit, visual evidence for bioturbation is present from 0–26 cm of the core (13.55–13.74 ka), despite relatively high sedimentation rates (100 cm/kyr). The radiocarbon age of the core top and evidence for bioturbation in the upper most sediments suggests that sedimentation rates declined substantially after 13.55 ka at this site. A nearby sediment core located in Sitka Sound to the southeast of the MEVF (EW0408-40JC) also records thick rhyolitic tephra and pyroclastic flow deposits consistent with the timing and geochemistry of the rhyolite deposit in EW0408-26JC (Addison et al., 2010). Many of the terrestrial sequences document extensive rhyolitic tephra and pyroclastic flow deposits among the younger MEVF volcanics (Riehle et al., 1992a, 1992b), indicating that this was one of the largest volumetric outpourings of the eruptive sequence. Two tephra analyzed from the trigger core EW0408-26TC at 6.5 cm (UA2176) and 47.5 cm (UA2177) are both geochemically identical (based on major elements) to the rhyolite deposit in EW0408-26JC at 29 cm (UA2168). Based on the isotope and radiocarbon stratigraphy of the trigger core (Fig. 2), it is likely that the rhyolite near the base of the trigger core (UA2177) either correlates with the rhyolite deposit at 13.78 ka in EW0408-26JC, or represents a geochemically similar eruption that occurred a few hundred years later (~13.34 ka), whereas the shallower deposit in the trigger core (UA2176) may reflect a compositionally similar rhyolitic eruption dating to the mid-Holocene (Addison et al., 2010); however, upward bioturbation of the 13.78 ka rhyolite is also a possibility.

Previous studies on land have documented only one dacite deposit near the top of the MEVF sequence (Riehle et al., 1992a; Beget and Motyka, 1998). Two samples analyzed in core EW0408-66JC, at 1375 cm and 859 cm, are rhyodacites. These samples are separated by 5 m in the core, which corresponds to ~400 yrs age difference. Sample UA2174 is dispersed in bioturbated sediment whereas UA2175 is a discrete tephra layer. The major-element geochemical composition of the two samples overlap, but the younger sample (UA2175) contains fewer rhyolitic shards and lower SiO_2 wt% values that provide an average dacitic major-element composition similar to published values of the MEd from land outcrops (Fig. 3, Fig. S3).

The stratigraphic placement of these tephra layers supports the geochemical correlation of sample UA2175 with terrestrial deposits described as the MEd. UA2175 is the uppermost tephra layer recorded in the EW0408 cores, similar to terrestrial observations. On land the MEd occurs just below a pollen zone of apparent Younger Dryas age that indicates cooling in southeast Alaska (Hansen and Engstrom, 1996). Similarly, sample UA2175 is just below evidence of a sustained ocean cooling in core EW0408-66JC (Fig. 5), whereas sample UA2174 is present just below a short-term cooling, followed by a longer-term warming. The inferred marine reservoir age of 600 yrs (resulting from the difference of the MEd age and the radiocarbon dates bracketing sample UA2175) is consistent with average marine reservoir estimates from the British Columbia coast for this time period (Southon and Fedje, 2003), and is supported by a "tuned" age model produced through correlation of foraminiferal $\delta^{18}O$ with the NGRIP Greenland $\delta^{18}O$ chronology (Praetorius and Mix, 2014). Therefore, stratigraphic, climatological, and geochemical data all indicate that sample UA2175 can be correlated with the MEd. The additional dacitic eruption that precedes the MEd by ~400 yr has not previously been recognized in any stratigraphic sequence, and warrants caution when employing the presumed MEd in sediments for correlation purposes without precise independent chronologic control or demonstrably complete stratigraphy.

3.2. Timing of volcanism

The tephra sequence presented here represents up to 22 individual eruptions from the MEVF, and indicates an age range of 14.6–13.1 ka for the interval of peak volcanism (Fig. 4). The onset of deglacial volcanic activity from Southeast Alaska coincides with the start of the Bølling–Allerød Interstade (BA) (Fig. 5), which is a widespread abrupt warming event in the Northern Hemisphere during the deglacial transition, essentially synchronous in Alaska and Greenland (Praetorius and Mix, 2014). The sea-surface warming of ~3 °C in the Gulf of Alaska (GOA) record occurs abruptly (in <90 yrs), consistent with ice-core records that register this transition as occurring within decades (Steffensen et al., 2008).

The start of the Southeast Alaska eruptive sequence presented here also follows rapidly behind the disappearance of ice-rafted debris (IRD) in the GOA marine sediments (Fig. 4), which constrains timing of the retreat of marine-terminating outlet glaciers onto land or into fjords behind shallow sills, in concert with abrupt warming at the onset of the BA (Davies et al., 2011). Although global eustatic sea level was rising throughout this time period (Lambeck et al., 2014), our surface loading model indicates a rapid fall in local relative sea level starting at ~14.5 ka due to isostatic rebound from regional glacial unloading (Fig. 4), which is consistent with observational data from nearby Icy Strait that indicates a rapid fall in relative sea level at ~14.2 ka (Mann and Streveler, 2008).

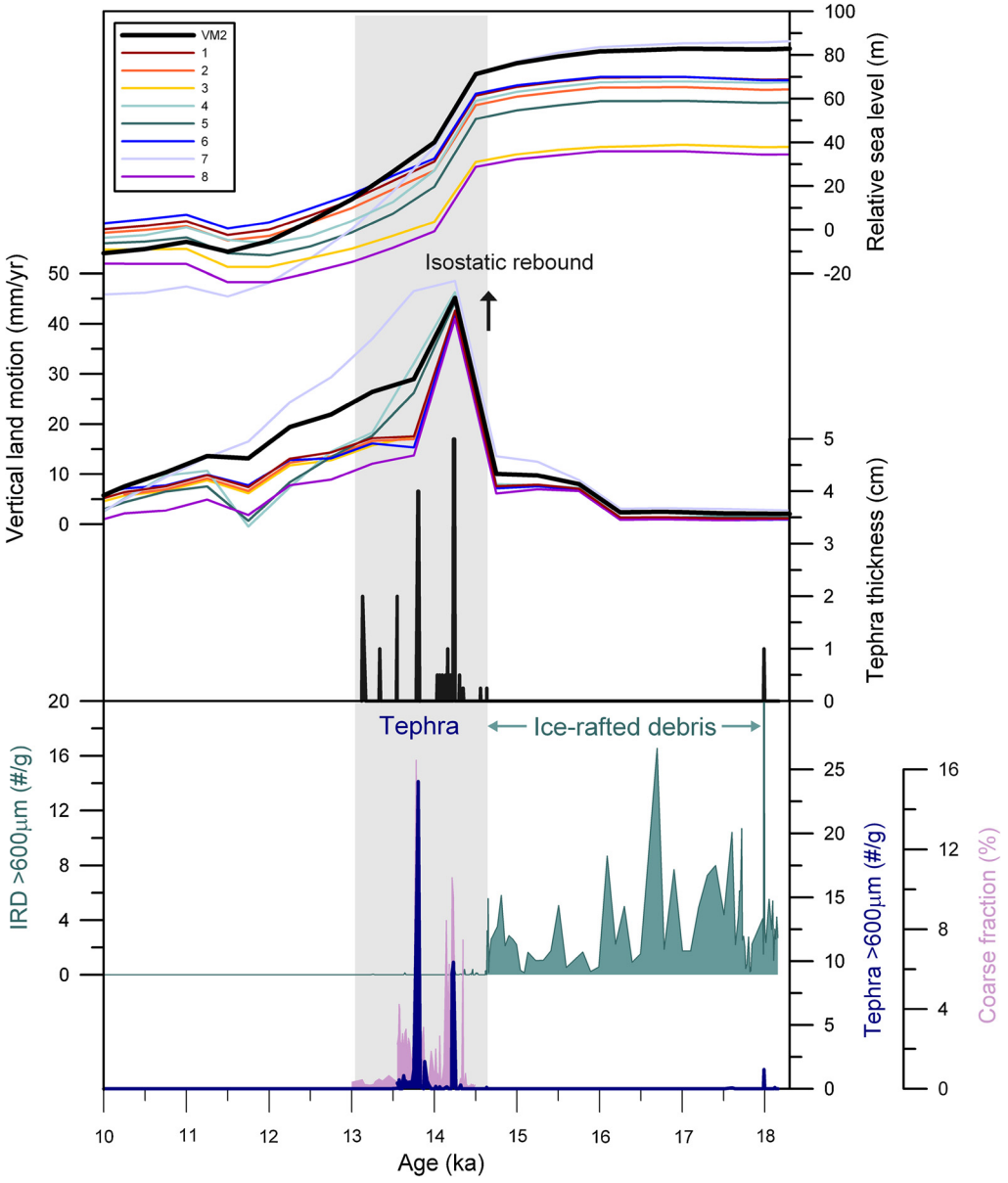

Fig. 4. Timing of the MEVF tephra sequence in relation to local deglaciation and isostatic adjustment. The upper panel shows model output of relative sea level (RSL) change at 57°N, 135°W, which is mainly controlled by vertical isostatic motion of the ocean floor in response to local deglaciation. The rate of ocean floor uplift at this location is also shown as this is a more direct indicator of time variations in the local stress field. Model output is shown for the ICE-5G ice loading history and a suite of viscosity models (Table S2) to sample uncertainty in this model input. Black RSL and uplift rate curves indicate model output generated using the VM2 Earth viscosity mode (see Section 2.6). Records of ice-rafted debris (IRD; green) and tephra grains >600 µm (dark blue) in the sediment samples are shown to depict the abrupt transition between ice-rafting and tephra deposition at 14.7 ka. Sand and gravel of this size can only be delivered by ice-rafting and tephra grains of this size point to a local source for volcanism. Light purple shading is the coarse fraction percent >125 µm that is dominated by volcanic tephra from 14.5–13.0 ka to show high abundance of ash grains between 125–600 µm in this interval. The onset of the volcanic sequence occurs near the disappearance of IRD from the marine sediments, and a rapid lowering of local relative sea level due to isostatic uplift in response to glacial unloading. (For interpretation of the references to color in this figure legend, the reader is referred to the web version of this article.)

The model output (Fig. 4) is shown as time series of RSL and rate of crustal uplift. The former gives vertical changes in sea-surface height (associated with changes in land ice volume and gravity) relative to the sea floor and can be compared to RSL reconstructions to test model accuracy. The latter gives a more direct estimate of regional solid Earth deformation and therefore changes in the regional stress field. RSL and uplift-rate curves were generated with several different Earth viscosity models to evaluate the sensitivity of the isostatic adjustment to a wide range of mantle viscosity values (Table S2), providing an estimate of uncertainty in this model input. While the results indicate a spread in the modeled amplitudes associated with the different viscosity values considered, the timing of rapid RSL fall and land uplift at ~14.5 ka is governed by the chronology of the adopted ice model (ICE-5G), which is consistent with the observed timing of glacial retreat out of the marine realm (Davies et al., 2011).

Sea level reconstructions in Southeast Alaska show regional heterogeneities due to the varying effects of isostatic depression from ice sheets on the mainland and the associated forebulge uplift effect that dominated at the outer coastal archipelagos (Shugar et al., 2014; Carlson and Baichtal, 2015). Our model results are compatible with the RSL constraints described in these studies. Most records from the outer coastal region of southeast Alaska show initiation of isostatic adjustment around ~14 ka (Shugar et al., 2014), implying rapid adjustments in the crust and shallow mantle. Thus, we find a rapid (nearly instantaneous) response of the onset of

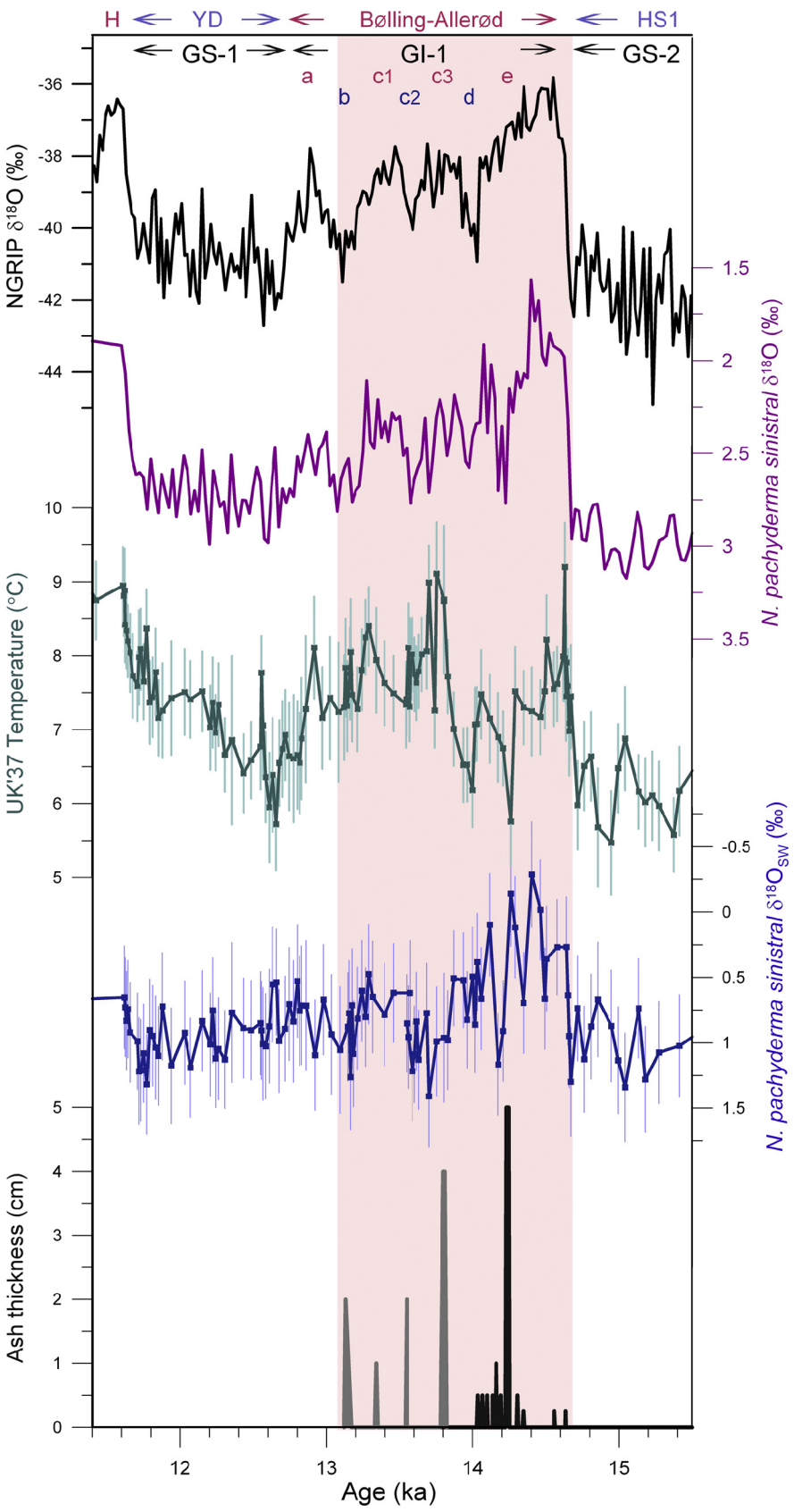

Fig. 5. Comparison of GOA and NGRIP climate and volcanic records. Data in order from the top: NGRIP $\delta^{18}O$ (Rasmussen et al., 2006; black), GOA planktonic (Nps) $\delta^{18}O$ composite record from cores EW0408-66JC and EW0408-26JC (Praetorius and Mix, 2014; violet), GOA alkenone temperature composite record (green), GOA $\delta^{18}O_{sw}$ (dark blue), and tephra thickness for basaltic (black) and rhyolitic or dacitic (gray) eruptions. Inter-site calibrations are detailed in the SI. Pink bar shows the interval of MEVF volcanic activity. The timing of major climate intervals are indicated at the top of the plot in their colloquial usage: Holocene (H; 11.6–0 ka), Younger Dryas (YD; 12.9–11.7 ka), Bølling–Allerød (14.6–12.9 ka), Heinrich Stadial 1 (HS1; 18–14.7 ka), and in the Greenland-specific chronology (Rasmussen et al., 2014). (For interpretation of the references to color in this figure legend, the reader is referred to the web version of this article.)

volcanism to unloading of overlying ice masses, related to major regional ice retreat and the associated isostatic adjustment. The end of the eruptive sequence similarly coincides with the slowdown of isostatic adjustment in the region.

Two plausible mechanisms could have linked the interval of isostatic adjustment with enhanced volcanism: 1) increased melt production generated through decompression in the shallow mantle (Maclennan et al., 2002), or 2) reduced storage time of crustal magmas through regional adjustment in crustal stress and enhanced dike formation (Jellinek et al., 2004; Rawson et al., 2016). The near-zero time-lag between regional isostatic adjustment and an abrupt increase in volcanic eruptive frequency in Southeast Alaska suggests the latter scenario is more plausible, or at least the dominant mechanism. Supporting this supposition is the rapid mobilization of differentiated magma through multiple vents. Decompression melting would not likely have produced differentiated magmas on the time-frames observed, while previous work by others has shown that the Mount Edgecumbe magma chamber likely contained cupolas above the main basaltic chamber that already contained the more siliceous material (e.g. Myers and Sinha, 1985; Riehle et al., 1992b).

The rapid response of the Southeast Alaska system contrasts with inferred lags of volcanism several thousand years behind sea-level rise in global compilations (Kutteroff et al., 2013; Watt et al., 2013). It is plausible to think that some volcanic systems may have longer lag times behind local unloading; for example, arc systems in thicker continental crust may have longer response times (Rawson et al., 2016) than relatively isolated volcanic systems with shallow magma chambers, such as in Southeast Alaska (Riehle et al., 1994). Nevertheless, our findings highlight the importance of well-constrained regional studies to understand the rates and sensitivity of interactions between surface processes and volcanic activity.

3.3. Regional climate change

Following the abrupt northern-hemisphere warming into the Bølling Interstade (14.7–14.6 ka locally based on our ^{14}C-dated alkenone paleotemperature reconstruction), progressive cooling off Southeast Alaska occurred in steps until ~14.0 ka; this interval largely corresponds with the interval of frequent basaltic/basaltic andesitic eruptions. A large δ^{18}O excursion (+1.0‰) that punctuates the Bølling interval in the GOA record from 14.25–14.18 ka occurred just after the deposition of a 5 cm thick basaltic tephra layer (UA2170) in core EW0408-26JC at 14.26 ka (Fig. 5). The marine temperature record documents a rapid cooling of 1.7 ± 0.6 °C coincident in timing (14.26–14.18 ka) with the δ^{18}O excursion, although the change in paleotemperature was initiated slightly prior to the increase in δ^{18}O (near the base of tephra layer UA2170). This abrupt cooling in GOA appears to precede the initiation of the GI-1d cold reversal in the NGRIP record. While changes in marine reservoir age could in principle account for the apparent age discrepancy in timing between similar events in Alaska and Greenland, we think it is more likely that this rapid cooling in the GOA records reflects a local climate perturbation. Based on our chronologic constraints, additional cooling events in the GOA are more closely aligned with the GI-1d, GI-1c2, and GI-1b events in Greenland.

A brief warming in the alkenone paleotemperatures commences at 13.87 ka, but the warming trend is punctuated by a rapid cooling event of 1.8 ± 0.5 °C just after deposition of the large rhyolitic eruption at 13.75 ka (UA2177). Another small cooling event (0.6 ± 0.5 °C) occurs in the alkenones after deposition of the tephra analyzed at 13.5 ka (UA2174) in core EW0408-66JC. However, this tephra is present within bioturbated sediments and occurs at the base of the core (1375 cm), so it is difficult to constrain the precise timing of tephra deposition relative to the paleotemperature change. Another cooling event of 1.0 ± 0.5 °C in the alkenones occurs from 13.24–13.17 ka, coinciding with the GI-1b event in Greenland. Brief warming occurs at 13.17 ka, followed by another cooling event of 0.6 ± 0.7 °C just after deposition of the tephra deposit in EW0408-66JC that is correlated with the MEd at 13.13 ka (UA2175). A 2.4 ± 0.7 °C cooling in the alkenones occurs from 12.9–12.7 ka, coincident with the Younger Dryas cold reversal in the NGRIP record. Thus, some abrupt multidecadal cooling events in the GOA appear to be associated with regional tephras, while others that clearly align with events in Greenland have no obvious association with tephra.

The $\delta^{18}O_{sw}$ reconstruction reveals low values, implying freshening of surface waters, between 14.6 and 14.0 ka. Although the rapid freshening of surface waters coincides with abrupt warming, the interval of freshening is not uniquely linked to the warmest temperatures, as there are intervals within the BA with equivalently high SSTs that do not show an apparent decrease in $\delta^{18}O_{sw}$. The interval with greatest apparent freshening and high variance in $\delta^{18}O_{sw}$ coincides with the interval of deposition of basaltic tephra, which is coeval with the rapid warming and disappearance of IRD at the onset of the Bølling Interstade (Fig. 5, Fig. S5). Although these initial tephra layers are thin (0.5 cm), the deposition of dark tephra in the ablation zone of glaciers could have reduced albedo of the snow and ice surfaces (Conway et al., 1996), thereby promoting rapid melting and accelerated local meltwater output along with deglaciation. This mechanism would likely have enhanced freshwater runoff into the Alaskan coastal currents during deglaciation, and this influx of low δ^{18}O water would in turn have influenced the isotopic composition of near-surface waters.

4. Discussion

Despite a high overall correlation between GOA and Greenland climate records throughout the deglacial interval (Praetorius and Mix, 2014), there are some discrepancies in the timing and structure of the decadal and centennial-scale cooling events within the BA. For example, the tuned GOA stable isotope record includes several isotopic excursions that coincide with the major climate reversals in NGRIP, such as the abrupt cooling events at ~14.0, 13.6, and 13.2 ka. The GOA climate record also documents additional events not recorded in NGRIP, such as the large cooling at 14.2 ka that occurs in stratigraphic proximity to the thickest basaltic tephra deposit. While there are many potential sources of regional climate variability during the deglaciation, differences in the pattern of climate fluctuations between the Gulf of Alaska and Greenland records could be explained in part by regional responses to volcanism and the tephra it produced. The interval of peak volcanic activity from 14.6–13.1 ka from Southeast Alaska coincides with some rapid fluctuations in the alkenone temperature record and with a prominent interval of high variance in the $\delta^{18}O_{sw}$ record in the GOA (Fig. S5).

Although firm attribution of specific causal relationships is difficult with only a few events, it is plausible that both hemispheric and regional forcings contribute to climate variability in the GOA region. While direct radiative-forcing effects from individual eruptions are unlikely to lead to long-term cooling due to the relatively short residence time of volcanic aerosols in the upper atmosphere (1–3 yrs), a prolonged increase in the frequency of eruptions could lead to either warming or cooling perturbations through ice-albedo, sea-ice, or CO_2 feedbacks. Modeling studies suggest that hemispheric cooling of decades to centuries can be initiated by the effects of multiple eruptions (McGregor et al., 2015; Pollack et al., 1993), or sea-ice feedbacks (Miller et al., 2012).

The integrated sulfate flux from Greenland provides a first-order measure of the combined Northern Hemisphere volcanic

forcing on centennial time scales (Fig. S6). This record differs slightly with the global compilation of Huybers and Langmuir (2009). Although the magnitude of individual sulfate peaks is greatest from ~13–7 ka, consistent with the global volcanic index, the sum of smaller volcanic events reveals intervals earlier in the deglacial sequence with frequent volcanism. The global compilations may favor silicic eruptions that are more explosive and thus provide distal tephra fallout that is more easily detected. If early post-glacial eruptions tend to be more mafic in composition, as is observed in Iceland and Southeast Alaska, these eruptions would likely be underrepresented in the global compilations due to the relatively limited extent of tephra fallout. Huybers and Langmuir (2009) also do not include small eruptions in their compilation. These omissions may skew the inferred timing of volcanism toward a younger mode, late in the deglaciation, and this in turn may bias estimates of the volcanic response time to unloading.

Sustained intervals of volcanism during the deglaciation may also have contributed to warming through increased CO_2 emissions (Huybers and Langmuir, 2009), and ice-albedo feedbacks. Tephra deposited in the ablation zone of glaciers accelerates melting because the tephra (>5 μm) tends to remain at the ice surface as the glacier retreats (Conway et al., 1996). Tephra that was once covered in the accumulation zone will at some point be uncovered in the ablation zone, where its growing concentration at the ice surface may provide a feedback for glacial melting in models (Peltier and Marshall, 1995). In some instances thick ash (>10 mm) can act as a short-term insulating layer on glaciers (Dragosics et al., 2016), delaying melting in areas proximal to the vent, but the wider dispersal of finer ash particles will likely more than compensate this localize insulating effect through a greater surface area over which thin tephra layers will act to increase ablation rates. Given the evidence for rapid retreat of marine terminating glaciers preceding/coinciding with the interval of frequent volcanic tephra deposition from the MEVF, it is plausible that tephra deposited on these regional glaciers would have an nearly immediate impact on melt rates in the already-expanding ablation zones. Thus, rapid responses of Alaskan volcanic systems to initial deglaciation may have accelerated ice losses in the region. The large number of volcanoes in the Pacific "Ring of Fire", coupled with the prevailing westerly winds, make deposition of tephra on the Laurentide and Cordilleran ice sheets (Fig. 1) a potential contributor to glacial wasting and ice-sheet instability.

Greenhouse gases are considered one of the powerful feedback mechanisms in the ice age cycle. Might deglacial volcanism contribute to this effect? The rise of atmospheric CO_2 during the first half of the deglaciation (18–15 ka) was likely sourced primarily from processes related to organic matter, as shown by $\delta^{13}C$ (Schmitt et al., 2012; Bauska et al., 2016), plausibly through a decrease in the net strength of the ocean's biological pump, which yields CO_2 depleted in ^{13}C relative to the atmosphere. Later in the deglaciation (<15 ka), further trends of rising CO_2 are not associated with long-term ^{13}C depletion, and therefore could include contributions from either ocean warming or volcanic CO_2, which both yield CO_2 rise not depleted in ^{13}C relative the background atmospheric values. Superimposed in these larger trends are abrupt (~10 ppm) rises in atmospheric CO_2 near 16–16.5 ka, 14.5–14.7 ka, and 11.5–12 ka (Marcott et al., 2014). Carbon isotope data from ice core CO_2 constrain the youngest and oldest of these abrupt rises to be sourced primarily from organic carbon reservoirs, most likely on land (Bauska et al., 2016), but could allow partial contributions from other sources including volcanic CO_2. The abrupt rise in atmospheric CO_2 near 14.7–14.5 ka, however, has no discernable change in atmospheric $\delta^{13}C$ (Bauska et al., 2016) implying that it cannot be sourced from oxidation of organic matter and therefore may be consistent with volcanic sources that responded relatively quickly to deglacial unloading.

5. Conclusions

Volcanism has the potential to both influence climate through emission of gases and ash particles, as well as respond to climate through pressure changes in shallow magma chambers related to glacial growth and demise. Here we document an episode of enhanced deglacial volcanic activity in Southeast Alaska, sourced primarily from the Mount Edgecumbe Volcanic Field, that coincided with rapid isostatic adjustment immediately following retreat of regional glaciers. This finding is consistent with the hypothesis that ice-unloading can trigger volcanism. We find no significant lag between the timing of major ice retreat and the onset of volcanism, suggesting that the volcanic response to deglaciation is rapid in this region. Between 14.6–13.1 ka, the MEVF exhibited an eruption recurrence interval of ~1.5 events/century based on the macroscopic tephra-fall units identified in this study. Early in the eruptive sequence, basaltic tephra is associated with surface-water freshening (implied by anomalously low $\delta^{18}O_{sw}$), suggesting that in this region, volcanism triggered by deglacial unloading may plausibly accelerate melting and water runoff through an albedo effect of dark tephra on snow and ice. With this insight from a well constrained regional study, re-examination of the integrated sulfate record from the Greenland ice core suggests that sustained early deglacial volcanism could accelerate rapid melting of some northern hemisphere glaciers through a reduction in surface albedo. Regional volcanism may thus play a significant role in century-to-millennial scale climate change during the deglaciation.

Acknowledgements

We thank K. Brewster for assistance with alkenone sample preparation and analysis measurements, J. Padman for assistance with marine sediment sample preparation, J. Pedro, C. Bacon, M. Clynne, and three anonymous reviewers for comments and suggestions that significantly improved the manuscript. This work was supported by NSF grants AGS-0602395 (Project PALEOVAR, ACM) and OCE-1204204 (A.C.M. and F.G.P.), and an NSF graduate research fellowship for S.K.P. J.A. was supported by the USGS Climate and Land Use Research & Development Program. Any use of trade, firm, or product names is for the descriptive purposes only and does not imply endorsement by the U.S. Government.

Appendix A. Supplementary material

Supplementary material related to this article can be found online at http://dx.doi.org/10.1016/j.epsl.2016.07.033.

References

Abbott, P.-M., Davies, S.-M., 2012. Volcanism and the Greenland ice-cores: the tephra record. Earth-Sci. Rev. 115, 173–191.

Addison, J.-A., Beget, J.-E., Ager, T.-A., Finney, B.-P., 2010. Marine tephrochronology of the Mt. Edgecumbe Volcanic Field, Southeast Alaska, USA. Quat. Res. 73, 277–292.

Alley, R.B., 2000a. The Younger Dryas cold interval as viewed from central Greenland. Quat. Sci. Rev. 19, 213–226.

Alley, R.B., 2000b. GISP2 – temperature reconstruction and accumulation data, NCDC-Paleoclimatology Online Files. https://www.ncdc.noaa.gov/paleo/study/2475 (accessed July 2016).

Bauska, T.-K., et al., 2016. Carbon isotopes characterize rapid changes in atmospheric carbon dioxide during the last deglaciation. Proc. Natl. Acad. Sci. USA 113, 3465–3470.

Beget, J.-E., Motyka, R.-J., 1998. New dates on late Pleistocene dacitic tephra from the Mount Edgecumbe volcanic field, southeastern Alaska. Quat. Res. 49, 123–125.

Bemis, B.-E., Spero, H.-J., Bijima, J., Lea, D.-W., 1998. Reevaluation of the oxygen isotopic composition of planktonic foraminifera: experimental results and revised paleotemperature equations. Paleoceanography 13 (2), 150–160.

Bourne, A.-J., et al., 2015. A tephra lattice for Greenland and a reconstruction of volcanic events spanning 25–45 ka b2k. Quat. Sci. Rev. 118, 122–141.

Bourne, A.J., et al., 2016. Underestimated risks of long-range ash dispersal from northern Pacific Arc volcanoes. Sci. Rep. 6, 29837. http://dx.doi.org/10.1038/srep29837.
Carlson, R.-J., Baichtal, J.-F., 2015. A predictive model for locating early Holocene archaeological sites based on raised shell-bearing strata in Southeast Alaska, USA. Geoarchaeology 30, 120–138.
Conway, H., Gades, A., Raymond, C.-F., 1996. Albedo of dirty snow during conditions of melt. Water Resour. Res. 32 (6), 1713–1718.
Coulter, S.-E., et al., 2012. Holocene tephras highlight complexity of volcanic signals in Greenland ice cores. J. Geophys. Res. 117, D21303.
Christie, W.-W., 2003. Lipid Analysis: Isolation, Separation, Identification and Structural Analysis of Lipids. The Oily Press.
Davies, M.-H., et al., 2011. The deglacial transition on the southeastern Alaska Margin: meltwater input, sea level rise, marine productivity, and sedimentary anoxia. Paleoceanography 26, PA2223.
Dragosics, M., et al., 2016. Insulation effects of Icelandic dust and volcanic ash on snow and ice. Arab. J. Geosci. 9, 126.
Dziewonski, A.-M., Anderson, D.-L., 1981. Preliminary reference Earth model. Phys. Earth Planet. Inter. 25, 297–356.
Eberlein, G.-D., Churkin, M., 1970. Tlevak Basalt, west coast of Prince of Wales Island, southeastern Alaska. In: Cohee, G.V., Bates, R.G., Wright, W.B. (Eds.), Changes in Stratigraphic Nomenclature by the U.S. Geological Survey, 1968. In: Geological Survey Bulletin 1294-A. United States Government Printing Office, Washington, DC, pp. 25–55.
Edwards, B.-R., Russell, J.-K., 2000. Distribution, nature, and origin of Neogene–Quaternary magmatism in the northern Cordilleran volcanic province, Canada. Geol. Soc. Am. Bull. 112, 1280–1295.
Goldfinger, C., 2011. Submarine paleoseismology based on turbidite records. Ann. Rev. Mar. Sci. 3, 35–66.
Greene, H.-G., O'Connell, V.-M., Brylinsky, C.-K., 2011. Tectonic and glacial related seafloor geomorphology as possible demersal shelf rockfish habitat surrogates—examples along the Alaskan convergent transform plate boundary. Cont. Shelf Res. 31, S39–S53.
Hammer, C.-U., Clausen, H.-B., Dansgaard, W., 1980. Greenland ice sheet evidence of post-glacial volcanism and its climate impact. Nature 288, 230–235.
Hansen, B.-C.-S., Engstrom, D.-R., 1996. Vegetation history of Pleasant Island, southeast Alaska, since 13,000 yr B.P. Quat. Res. 46, 161–175.
Horn, D.R., Delach, M.N., Horn, B.M., 1969. Distribution of volcanic ash layers and turbidites in the North Pacific. Geol. Soc. Am. Bull. 80 (9), 1715–1724.
Huybers, P., Langmuir, C., 2009. Feedback between deglaciation, volcanism, and atmospheric CO_2. Earth Planet. Sci. Lett. 286, 479–491.
Jellinek, A.M., Manga, M., Saar, M.O., 2004. Did melting glaciers cause volcanic eruptions in eastern California? Probing the mechanics of dike formation. J. Geophys. Res. 109, B09206. http://dx.doi.org/10.1029/2004JB002978.
Jensen, B.-J.-L., Froese, D.-G., Preece, S.-J., Westgate, J.-A., Stachel, T., 2008. An extensive middle to late Pleistocene tephrochronologic record from east-central Alaska. Quat. Sci. Rev. 27, 411–427.
Jensen, B.-J., et al., 2014. Transatlantic distribution of the Alaskan White River Ash. Geology 42 (10), 875–878. http://dx.doi.org/10.1130/G35945.1.
Kendall, R., Mitrovica, J.-X., Milne, G.-A., 2005. On post-glacial sea level – II. Numerical formulation and comparative results on spherically symmetric models. Geophys. J. Int. 161, 679–706.
Kuehn, S.-C., Froese, D.-G., Shane, P.-A.-R., 2011. The INTAV intercomparison of electron-beam microanalysis of glass by tephrochronology laboratories, results and recommendations. Quat. Int. 246, 19–47.
Kutteroff, S., et al., 2013. A detection of Milankovitch frequencies in global volcanic activity. Geology 41, 227–230.
Lambeck, K., Rouby, H., Purcell, A., Sun, Y., Sambridge, M., 2014. Sea level and global ice volumes from the Last Glacial Maximum to the Holocene. Proc. Natl. Acad. Sci. USA 111, 15296–15303.
Langmann, B., Zaksek, K., Hort, M., Duggen, S., 2010. Volcanic ash as fertiliser fort the surface ocean. Atmos. Chem. Phys. 10, 3891–3899.
LeBas, M.-J., Lemaitre, R.-W., Streckeisen, A., Zanettin, B., 1986. A chemical classification of volcanic rocks based on the total alkali silica diagram. J. Petrol. 27, 745–750.
Maclennan, J., et al., 2002. The link between volcanism and deglaciation in Iceland. Geochem. Geophys. Geosyst. 3 (11), 1062.
Mann, D.-H., Streveler, G.-P., 2008. Post-glacial relative sea level, isostasy, and glacial history in Icy Strait, Southeast Alaska, USA. Quat. Res. 69, 201–216.
Marcott, S.-A., et al., 2014. Centennial-scale changes in the global carbon cycle during the last deglaciation. Nature 514, 616–619.
McCormick, M.-P., Thomason, L.-W., Trepte, C.-R., 1995. Atmospheric effects of the Mt Pinatubo eruption. Nature 373, 399–404.
McGregor, H.-V., et al., 2015. Robust global ocean cooling trend for the pre-industrial Common Era. Nat. Geosci. 8, 671–678.
Myers, J.-D., Sinha, A.-K., 1985. A detailed Pb isotopic study of crustal contamination/assimilation: the Edgecumbe volcanic field. Geochim. Cosmochim. Acta 49, 1343–1355.
Miller, G., et al., 2012. Abrupt onset of the Little Ice Age triggered by volcanism and sustained by sea-ice/ocean feedbacks. Geophys. Res. Lett. 39, L02708.
Milne, G.-A., Mitrovica, J.-X., 1998. Postglacial sea-level change on a rotating Earth. Geophys. J. Int. 133, 1–19.
Mitrovica, J.-X., Milne, G.-A., 2003. On post-glacial sea level – I. General theory. Geophys. J. Int. 154, 253–267.
Mitrovica, J.-X., Wahr, J., Matsuyama, I., Paulson, A., 2005. The rotational stability of an ice-age earth. Geophys. J. Int. 161, 491–506.
Mortensen, A.-K., et al., 2005. Volcanic ash layers from the Last Glacial Termination in the NGRIP ice core. J. Quat. Sci. 20 (3), 209–219.
Peltier, W.R., Marshall, S., 1995. Coupled energy-balance/ice-sheet model simulations of the glacial cycle: a possible connection between terminations and terrigenous dust. J. Geophys. Res. 100 (D7), 14,269–14,289.
Peltier, W.R., 2004. Global glacial isostasy and the surface of the ice-age earth: the ICE-5G (VM2) model and GRACE. Annu. Rev. Earth Planet. Sci. 32, 111–149.
Pollack, J.-B., Rind, D., Lacis, A., Hansen, J.-E., Sato, M., Reudy, R., 1993. GCM simulations of volcanic aerosol forcing. Part 1: Climate changes induced by steady-state perturbations. J. Climate 6, 1719–1742.
Praetorius, S.-K., Mix, A.-C., 2014. Synchronization of North Pacific and Greenland climates preceded abrupt deglacial warming. Science 345, 444–448.
Prahl, F.-G., Muehlhausen, L.-A., Zahnle, D.-L., 1988. Further evaluation of long-chain alkenones as indicators of paleoceanographic conditions. Geochim. Cosmochim. Acta 52, 2303–2310.
Rasmussen, S.-O., et al., 2006. A new Greenland ice core chronology for the last glacial termination. J. Geophys. Res. 111, D06102.
Rasmussen, S.-O., et al., 2014. A stratigraphic framework for abrupt climatic changes during the Last Glacial period based on three synchronized Greenland ice-core records: refining and extending the INTIMATE event stratigraphy. Quat. Sci. Rev. 106, 14–28.
Rawson, H., et al., 2016. The magmatic and eruptive response of arc volcanoes to deglaciation: insights from southern Chile. Geology 44, 251–254.
Reimer, P.-J., et al., 2013. INTCAL13 and MARINE13 radiocarbon age calibration curves, 0–50,000 years cal BP. Radiocarbon 55, 1869–1887.
Riehle, J.-R., et al., 1992a. The Mount Edgecumbe tephra deposits, a marker horizon in southeastern Alaska near the Pleistocene–Holocene Boundary. Quat. Res. 37, 183–202.
Riehle, J.-R., Champion, D.-E., Brew, D.-A., Lanphere, M.-A., 1992b. Pyroclastic deposits of the Mount Edgecumbe volcanic field, southeast Alaska: eruptions of a stratified magma chamber. J. Volcanol. Geotherm. Res. 53, 117–143.
Riehle, J.-R., Budahn, J.-R., Lanphere, M.-A., Brew, D.-A., 1994. Rare-earth-element contents and multiple mantle sources of the transform-related Mount Edgecumbe basalts, southeastern Alaska. Can. J. Earth Sci. 31, 852–864.
Robock, A., 2000. Volcanic eruptions and climate. Rev. Geophys. 38, 191–219.
Robock, A., 2002. Pinatubo eruption: the climatic aftermath. Science 295, 1242–1244.
Schmitt, J., et al., 2012. Carbon isotope constraints on the deglacial CO_2 rise from ice cores. Science 336, 711–714.
Shugar, D.-H., et al., 2014. Post-glacial sea level rise along the Pacific coast of North America. Quat. Sci. Rev. 97, 170–192.
Souther, J.-G., 1992. The late Cenozoic Mount Edziza volcanic complex, British Columbia. Geol. Surv. Can. Mem. 420, 320 p.
Southon, J.-R., Fedje, D., 2003. A post-glacial record of ^{14}C reservoir ages for the British Columbia coast. Can. J. Archeol. 27, 95–111.
Steffensen, J.-P., et al., 2008. High-resolution Greenland ice core data show abrupt climate change happens in few years. Science 321, 680–684.
Waelbroeck, C.-L., et al., 2002. Sea-level and deep water temperature changes derived from benthic foraminifera isotopic records. Quat. Sci. Rev. 21, 295–305.
Walinsky, S.-E., et al., 2009. Distribution and composition of organic matter in surface sediments of coastal Southeast Alaska. Cont. Shelf Res. 29, 1565–1579.
Watt, S.-F.-L., Pyle, D.-M., Mather, T.-A., 2013. The volcanic response to deglaciation: evidence from glaciated arcs and a reassessment of global eruption records. Earth-Sci. Rev. 122, 77–102.
Welchman, R.-A., 2012. Bringing the world to a standstill: an investigation into the effects of a Novarupta scale volcanic eruption on today's aviation industry. Alaska Park Sci. 11, 82–87.
Zielinski, G.-A., et al., 1996. A 110,000-yr record of explosive volcanism from the GISP2 (Greenland) ice core. Quat. Res. 45, 109–118.
Zielinski, G.-A., et al., 1997. Volcanic aerosol records and tephrochronology of the Summit, Greenland, ice cores. J. Geophys. Res. 102, 26,625–26,640.